ADVANCED MATERIALS

Supporting Information

for *Adv. Mater.*, DOI 10.1002/adma.202310237

Trace Water in Lead Iodide Affecting Perovskite Crystal Nucleation Limits the Performance of Perovskite Solar Cells

Renjun Guo, Qiu Xiong, Aleksander Ulatowski, Saisai Li, Zijin Ding, Tianxiao Xiao, Suzhe Liang, Julian E. Heger, Tianfu Guan, Xinyu Jiang, Kun Sun, Lennart K. Reb, Manuel A. Reus, Andrei Chumakov, Matthias Schwartzkopf, Minjian Yuan, Yi Hou, Stephan V. Roth, Laura M. Herz, Peng Gao and Peter Müller-Buschbaum**

Supporting Information

Trace water in lead iodide affecting perovskite crystal nucleation limits the performance of perovskite solar cells

Renjun Guo [†], Qiu Xiong [†], Aleksander Ulatowski, Saisai Li, Zijin Ding, Tianxiao Xiao, Suzhe Liang, Julian E. Heger, Tianfu Guan, Xinyu Jiang, Kun Sun, Lennart K. Reb, Manuel A. Reus, Andrei Chumakov, Matthias Schwartzkopf, Minjian Yuan, Yi Hou, Stephan V. Roth, Laura M. Herz, Peng Gao, Peter Müller-Buschbaum**

Correspondence to: peng.gao@fjirsm.ac.cn; muellerb@ph.tum.de.

This file includes:

Supplemental Experimental Procedures 1-8
Supplementary Fig. 1 to 24
Tables S1 to S8

Supplemental Experimental Procedures

Supplementary Note 1: Calculation of water content in lead iodide precursors

The water contents in lead iodide precursors are calculated by parts per million, which is defined by the parts per million ratio of the mass of the solute to the mass of the total solution, as shown below:

$$parts\ per\ million\ =\ \frac{the\ mass\ of\ solute}{the\ mass\ of\ total\ precusor} * 10^6$$

Supplementary Note 2: Jeziorny equation

The Jeziorny equation is defined as follows to describe the relationship of temperature–time–transformation during non-isothermal crystallization:

$$X_t = 1 - e^{-Z_t t^n}. \quad (1)$$

Where X_t is the fractional crystallinity at the time t; Z_t is the rate constant, and n is the Jeziorny exponent representing the mechanism of nucleation and geometry of growth.

Through a transformation using the logarithm function, we can obtain the following:

$$\ln[-\ln(1 - X_t)] = \ln Z_t + n \ln t \quad (2)$$

In which X_t is the fraction of transformed material after a hold time. After fitting with the raw data, we could obtain a straight line with slope n and the intercept $\ln Z_t$.

Finally, the rate constant is corrected by the heating rate φ:

$$\lg Z_c = \lg Z_t / \varphi \quad (3)$$

Supplementary Note 3: Continuous variations method

A series of solutions are prepared where the total moles of material (PbI_2) and ligand (DMSO) are as shown in Table S1-S3, n_{total}, in each solution remained the same:

$$n_{total} = n_M + n_L \quad (4)$$

Where and n_L are the moles of PbI_2 and DMSO separately.

The relative amount of PbI_2 and DMSO in each solution is expressed as the mole fraction of DMSO, X_L and the mole fraction of PbI_2, X_M,.

$$X_L = \frac{n_L}{n_{total}} \quad (5)$$

$$X_M = 1 - \frac{n_L}{n_{total}} \quad (6)$$

PbI_2·DMSO complex shows the absorption peak at 380 nm in previous reports, which we use to record the X_L as a function of absorption.[1] The maximum absorbance in the graph of absorbance versus X_L can be used to calculate the coordination number n through the below equation:

$$n = \frac{X_L}{1 - X_L} \quad (7)$$

The absorbance at 380 nm also includes the absorbance of PbI_2 and PbI_2·DMSO complex; thus, a calibration of absorbance is executed to eliminate the effects induced by the absorbance of PbI_2 by a reduction in the PbI_2 absorbance background.

We assume that the concentration of PbI_2 and DMSO are $\boldsymbol{a}$ and $\boldsymbol{b}$, and the concentration of the equilibrium status for the PbI_2·DMSO complex is X, we could obtain the equilibrium constant through equation (7):

$$K = \frac{X}{(a-X)(b-X)} \tag{8}$$

After calibration of absorbance, we can regard that the absorbance is proportional to the concentration of the PbI_2·DMSO complex. By keeping constant moles of PbI_2 and DMSO, we can find that one absorbance point corresponds to two different DMSO concentrations. We assume that the concentrations of relative PbI_2 and DMSO are a_1, a_2 and b_1 b_2, then we could obtain the equilibrium constant for the PbI_2·DMSO complex via equation (8):

$$K = \frac{X}{(a_1-x)(b_1-nx)} = \frac{X}{(a_2-x)(b_2-nx)} \tag{9}$$

Thus, we prepare the solutions by mixing PbI_2 and DMSO, as shown in Table. S2-S3, in which concentration is diluted to half as aforementioned solutions.

Supplementary Note 4: Absorption spectrum data analysis

The optical depth α of the films was calculated from the reflection-corrected transmissivity of the films as

$$\alpha = \ln\left(\frac{1-R}{T}\right) \tag{10}$$

where R and T are the fractions of the reflected and transmitted light through the sample, respectively. The optical depth spectrum was offset vertically to 0 below the bandgap, to account for different amounts of scattering in the films.

Supplementary Note 5: Optical-pump—THz-probe data analysis

The photoinduced change of conductivity, $\Delta\sigma$, is calculated from the relative change of THz probe transmission, $\frac{\Delta T}{T}$, according to Tinkham's formula [2-4]

$$\Delta\sigma = -\frac{\Delta T}{T}\left(\frac{\epsilon_0 c(1+n_{sub})}{L}\right) \tag{11}$$

where $\frac{\Delta T}{T} = \frac{T_{photoexcited} - T_{dark}}{T_{dark}}$ is the difference between THz electric field transmission through a photoexcited thin film sample and the same sample in the dark, divided by the THz field transmission through the sample in the dark. ϵ_0 is the permittivity of free space, c is the speed of light, n_{sub}=2.1 is the refractive index of the quartz substrate at THz frequencies and L is

the thickness of the thin film, measured with a Dektak profilometer to be 600±20 nm for all the films.[5]

The photoinduced change of conductivity is assumed to be caused by the presence of photoinjected charge carriers with electron-hole pair density n and sum charge-carrier mobility μ,

$$\Delta\sigma = \mu e n \tag{12}$$

where e is the electron charge. Combining equations 9 and 10, the mobility of the material can be calculated from the relative change of the probe's transmission at time=0, by estimating the number of photoinjected charge-carrier pairs, $n(t=0)$ from absorption data,

$$n(t=0) = \frac{F(1-R_{pump}-T_{pump})\phi}{E_{photon}L} \tag{13}$$

Here, F is the fluence of the photoexcitation, R_{pump} and T_{pump} are the fractions of reflected and transmitted light at the pump's wavelength obtained from absorption measurements, E_{photon} is the energy of a single photon at the pump's wavelength, L is the thickness of the thin-film sample, and Φ is the branching ratio of absorbed photons-to-charge-carrier pairs. Φ is assumed to be 1 due to a low value of exciton binding energy in these materials.[6].

The decay of the photoconductivity with time after photoexcitation is caused by the recombination of free charge-carrier pairs that happens via three main decay paths: trap-assisted recombination (with rate k_1), radiative recombination of electrons and holes (with decay constant k_2) and many-body (Auger) decay (with characteristic constant k_3), according to the equation 12[7]:

$$\frac{dn}{dt} = -k_1 n - k_2 n^2 - k_3 n^3 . \tag{14}$$

The decay dynamics of the photoexcited charge carriers can be obtained by fitting the solution of the differential equation 12 to the decay traces of photoconductivity. Due to the relatively low fluences ($F \leqslant 25$ μJ/cm^2) and low charge-carrier densities used in this study, Auger recombination did not contribute to the charge-carrier decay dynamics. It was omitted in the model used for fitting. Since the measurement window of OPTP measurements is only about 1ns long, the contribution from the slow monomolecular recombination can also be neglected, leaving only the bimolecular recombination rate in the model accounting for the fluence dependence of the dynamics.

The solution to equation (11), with k_1 and k_3 set to 0, was fitted globally for each sample to the photoconductivity decay traces for all photoexcitation fluences used. The value of the bimolecular recombination constant k_2 was then extracted from the fitting parameters. The charge-carrier sum mobility μ has been obtained from the relative transmission of the THz probe at time=0, as summarized above, using the variation between values obtained from different photoexcitation fluences as the uncertainty of the measurement.

The photoconductivity measurements show a slight decrease in the effective bimolecular recombination constant k_2 with increased water concentration, which could be caused by increased photon retention in the films with higher water contamination.[8] Morphological

changes in the films could cause higher photon retention and would increase photon recycling effects (the phenomenon where photons emitted during bimolecular recombination are re-absorbed in the film, generating another free electron-hole pair), which prolongs the effective decay lifetime of the photoconductivity.

Supplementary Note 6: TRPL data analysis

The photoluminescence decay is dominated by monomolecular (trap-assisted) charge-carrier recombination, which results in mono-exponential decay dynamics. Monomolecular recombination is expected to dominate the charge-carrier dynamics for low excitation fluence, such as the one used in this measurement (resulting in very low bimolecular recombination strength), measured over a long-time window (2μs). Since the density of photoexcited charge carriers under solar illumination is similar to or lower than in the presented TRPL measurement, the monomolecular recombination rate k_1 obtained from the TRPL data is most relevant for solar cell applications.

The decay rate of the charge-carrier population was obtained from TRPL decays by fitting a mono-exponential function (solution to equation 12 with k_2=k_3=0) to the data. Since the steady PL spectra arise from bimolecular recombination, its intensity is proportional to the product of electron (n) and hole (p) populations, which are assumed to be equal in an undoped, photoexcited semiconductor,

$$PL \propto k_2 np = k_2 n^2 = k_2 e^{-2k_1 t} \tag{15}$$

hence, the decay rate of the charge-carrier population is extracted as half the decay rate of the PL signal obtained from the mono-exponential fits.

Supplementary Note 7: The calculation of the density of trap-assistant centers

The density of the trap-assistant center is simulated by solving equation 15.

$$N_t = \frac{1}{k_1 \tau} \tag{16}$$

Where $\boldsymbol{k}_1$ is the trap-assisted recombination rate obtained from TRPL measurement, and τ is the average lifetime of the non-radiative carriers.

Supplementary Note 8: Mobility calculation via space-charge limited current measurements

The mobility value is typically extracted from the quadratic region of the dark current-voltage curve by fitting the Mott-Gurney equation:

$$I = \frac{9}{8} \varepsilon_0 \varepsilon \mu S \frac{(V - V_{BI})^2}{L^3} \tag{17}$$

where I is the current, V and V_{BI} are the applied and built-in voltage, and ε is the permittivity of perovskite materials, L is the thickness of the perovskite film which is measured by a Dektak profilometer, and μ is the charge carrier mobility, S is the area of the electrode. The detailed parameters are listed in the Table. S6. [9-11]

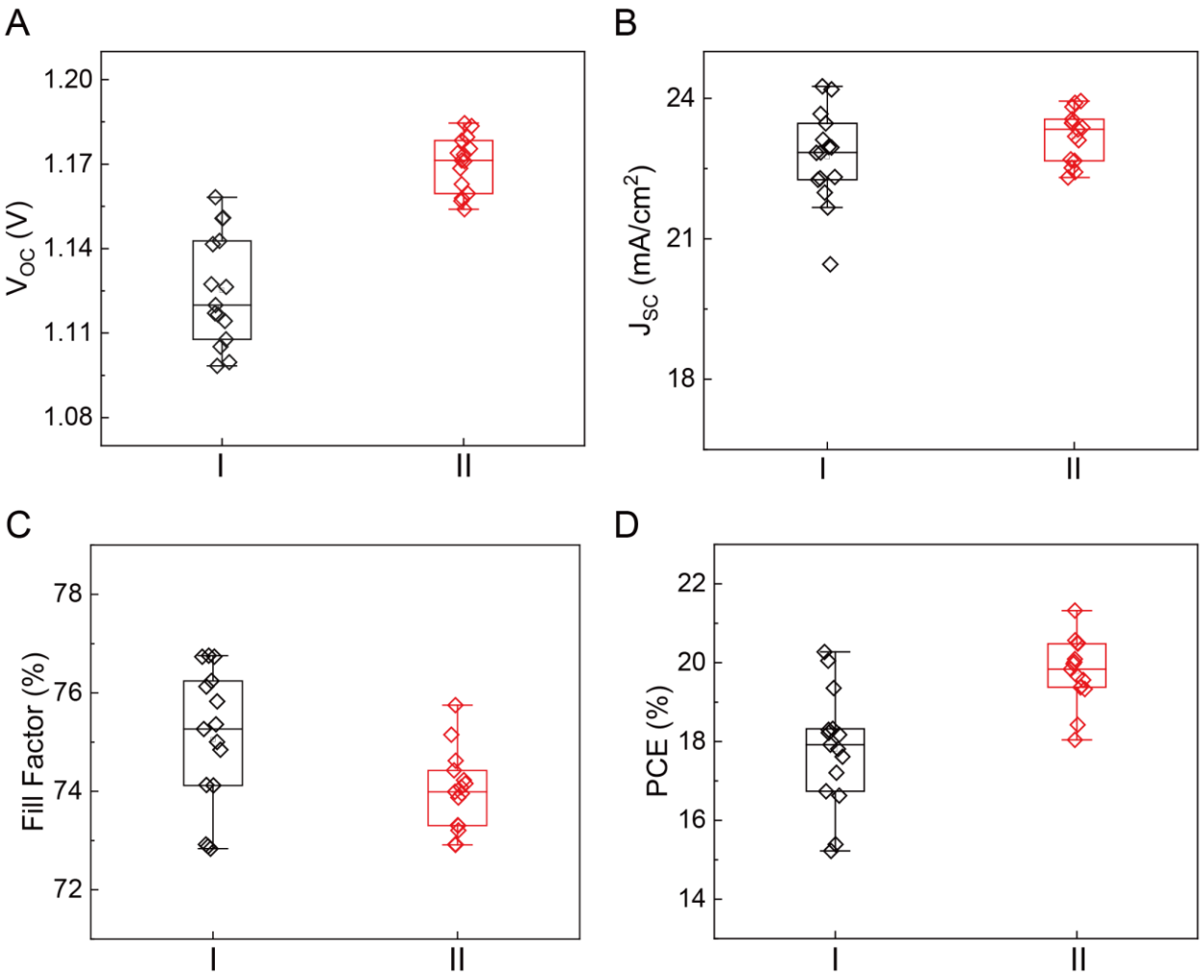

Figure S1.

Statistical performance of the full batch of 15 one-step antisolvent fabricated $(MAPbBr_3)_{0.17}(FAPbI_3)_{0.83}$ perovskite solar cells based on type I (solution synthesis) and type II (high-temperature synthesis) PbI_2. (A) open-circuit voltage; (B) short-circuit current; (C) fill factor; (D) power conversion efficiency.

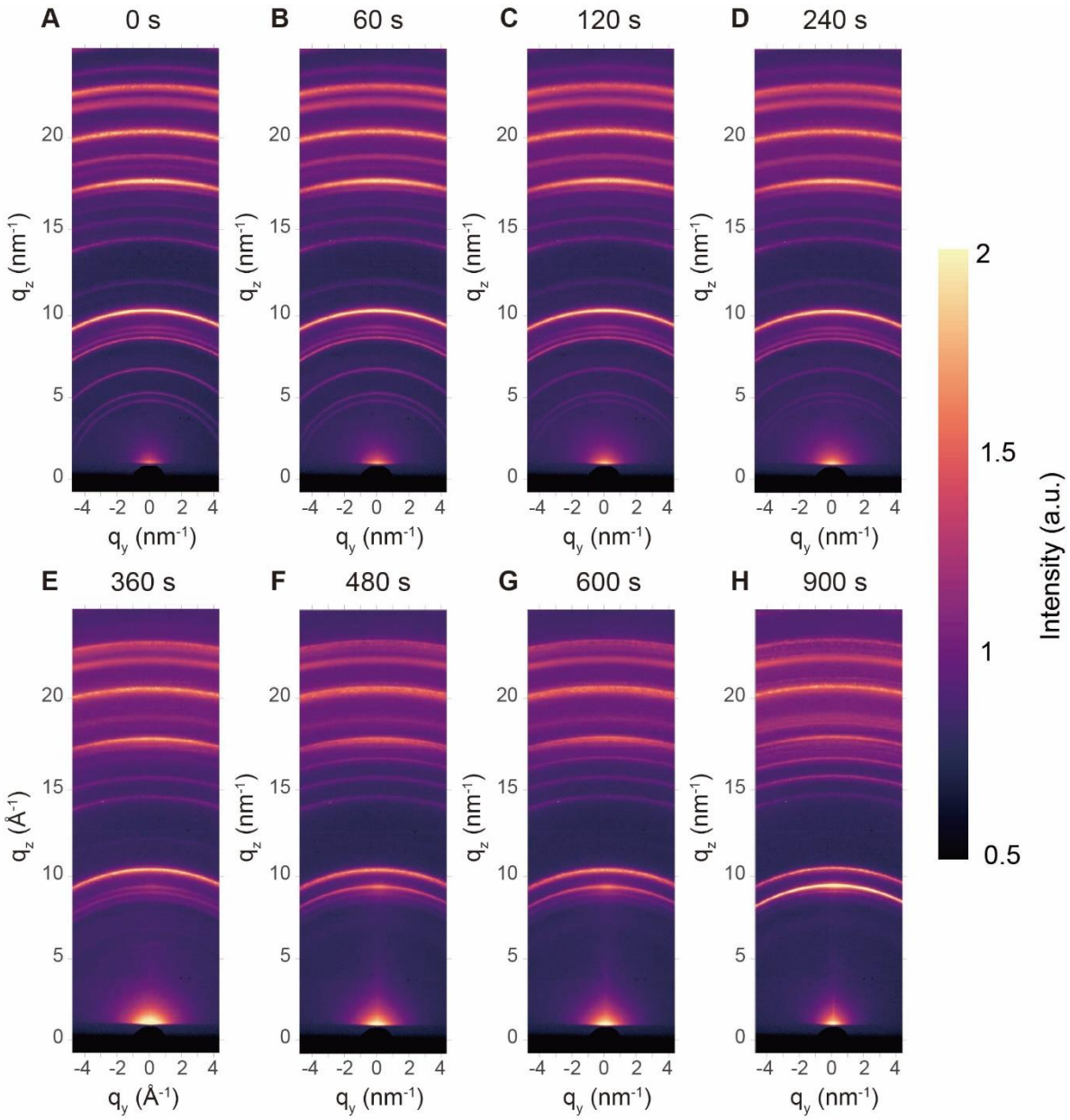

Figure S2.

Evolution of 2D GIWAXS data for perovskite films with 0 ppm water in situ annealed at 150 °C. (A) 0 s; (B) 60 s; (C) 120 s; (D) 240 s; (E) 360 s; (F) 480 s; (G) 600 s; (H) 900 s.

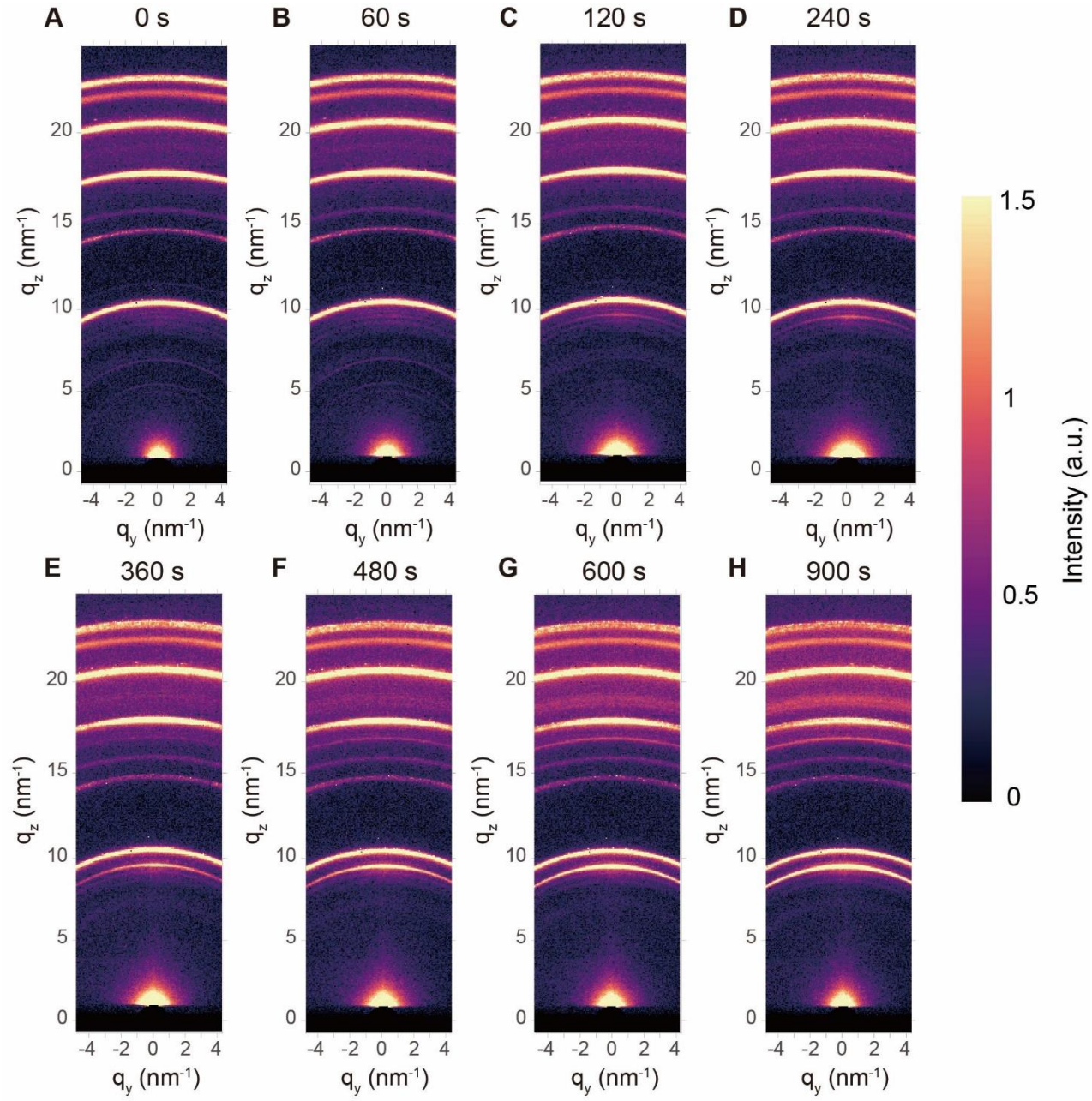

Figure S3.

Evolution of 2D GIWAXS data for perovskite films with 70 ppm water in situ annealed at 150 °C. (A) 0 s; (B) 60 s; (C) 120 s; (D) 240 s; (E) 360 s; (F) 480 s; (G) 600 s; (H) 900 s.

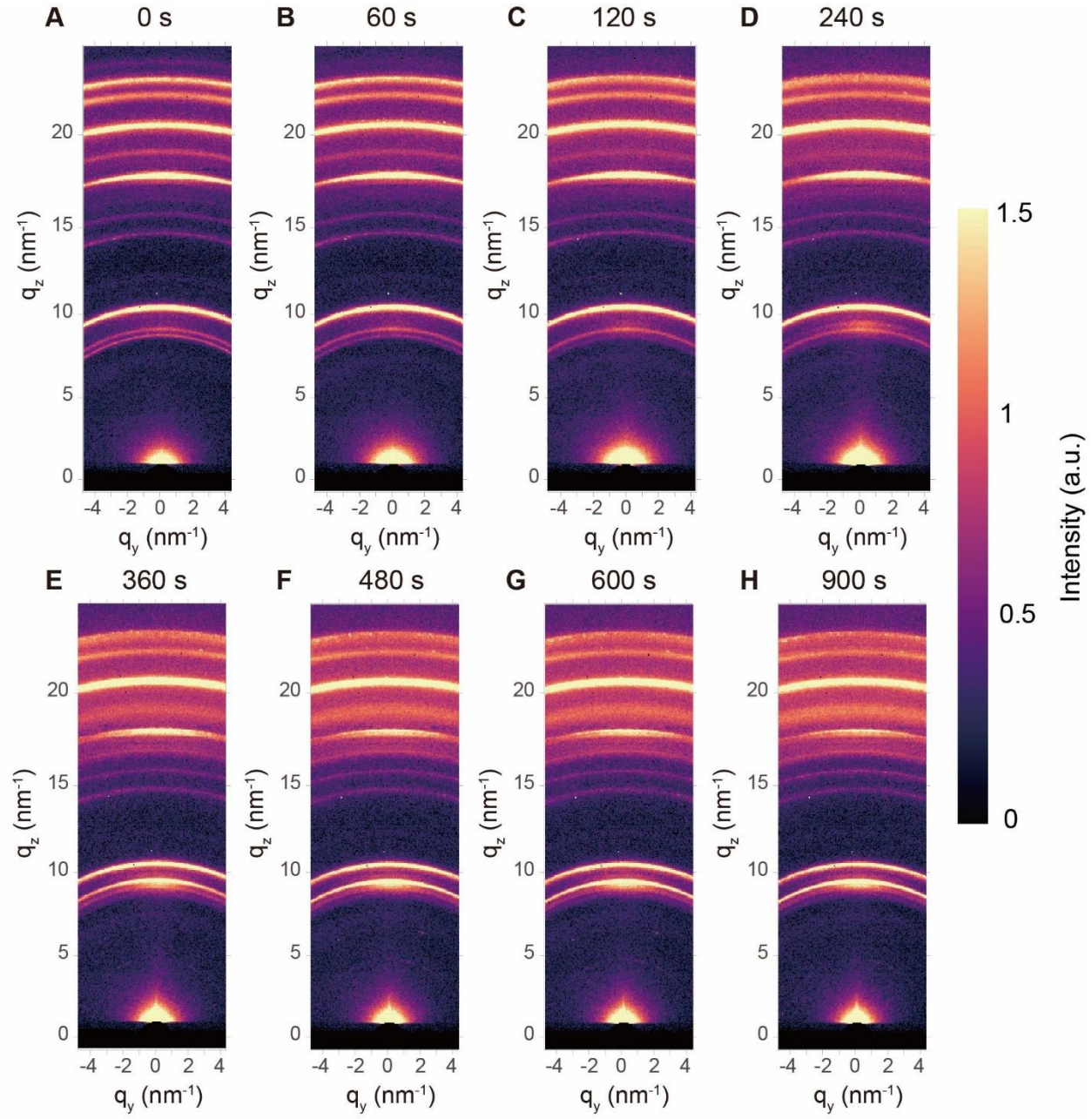

Figure S4.

Evolution of 2D GIWAXS data for perovskite films with 700 ppm water in situ annealed at 150 °C. (A) 0 s; (B) 60 s; (C) 120 s; (D) 240 s; (E) 360 s; (F) 480 s; (G) 600 s; (H) 900 s.

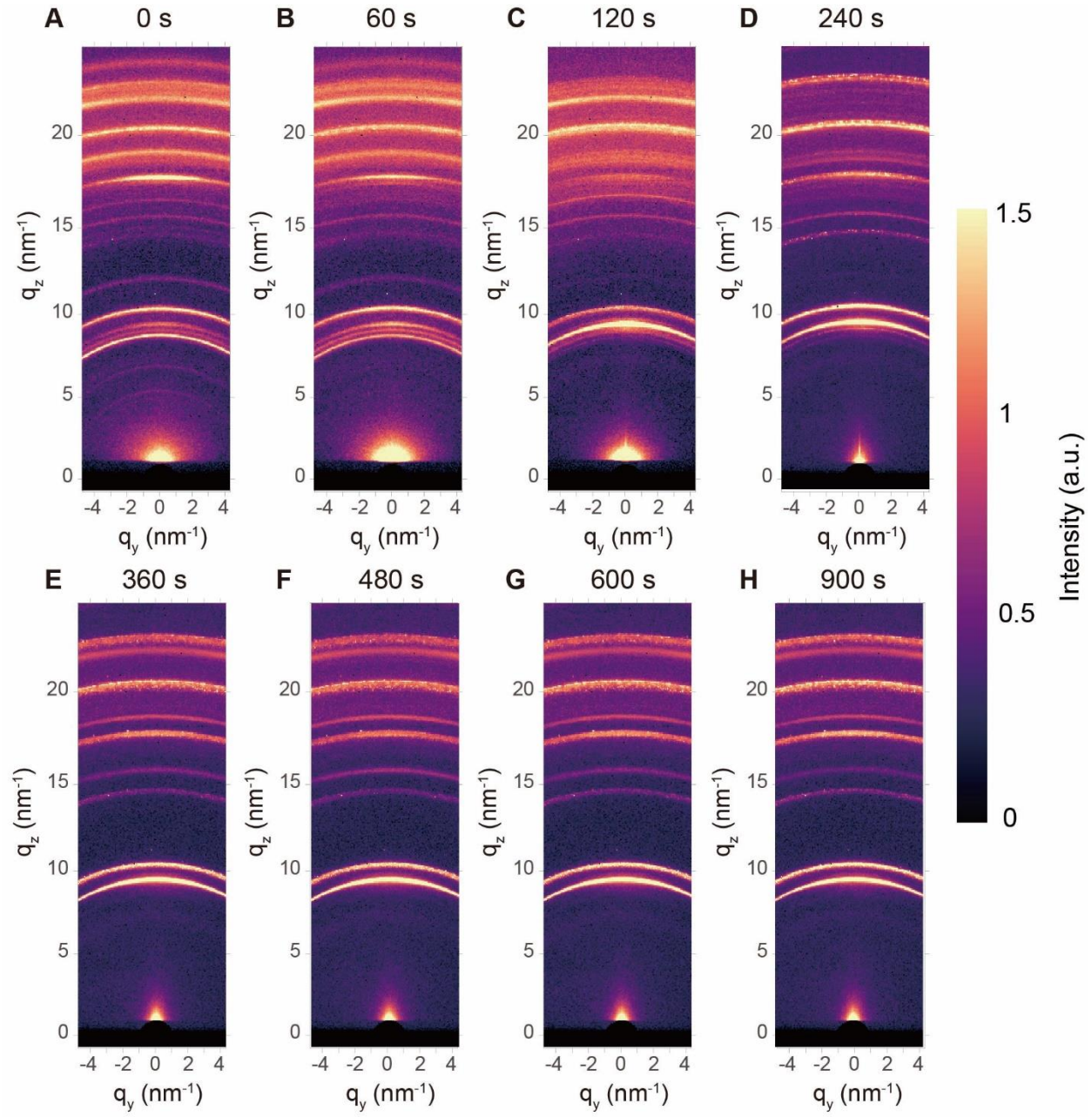

Figure S5.

Evolution of 2D GIWAXS data for perovskite films with 7000 ppm water in situ annealed at 150 °C. (A) 0 s; (B) 60 s; (C) 120 s; (D) 240 s; (E) 360 s; (F) 480 s; (G) 600 s; (H) 900 s.

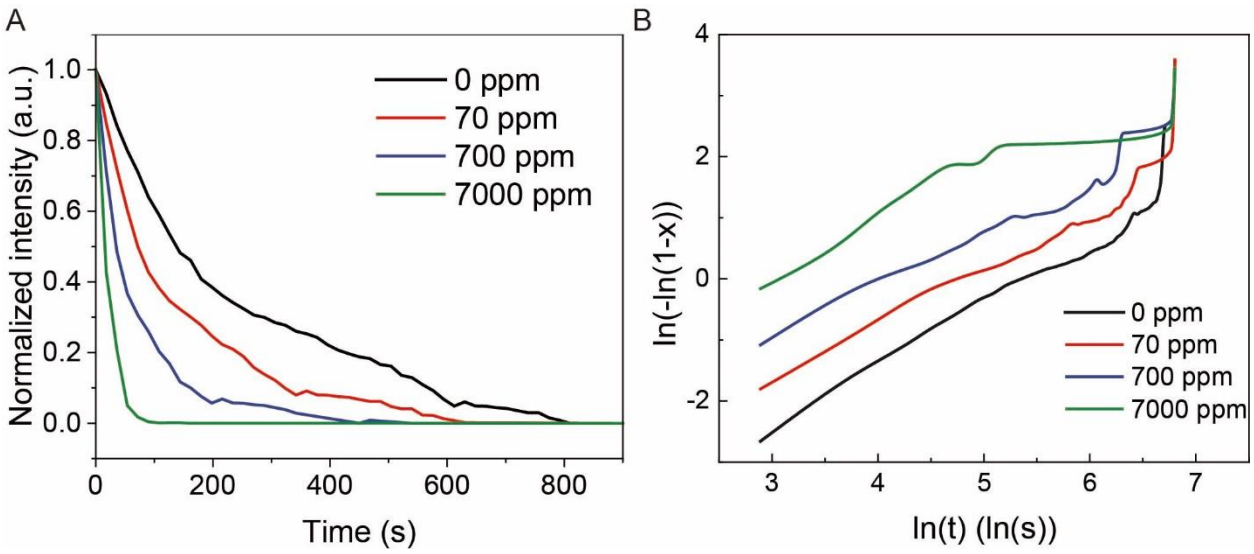

Figure S6. Data evaluation from Jeziorny equation.

(a) Temporal evolution of the perovskite-related complex Bragg peak q = 6.5 nm^{-1} intensity of perovskite films with different amounts of water contents during annealing. (b) Experimental data extracted from 0, 70, 700, and 7000 ppm of perovskite films at the peak with q = 6.5 nm^{-1} fitted to the Jeziorny equation, and Z_c indicates the crystallization rate, which is subtracted by the method mentioned in Supplementary Note 1 and calculated in Table S4. The lower constant rate indicates a slower crystallization process.

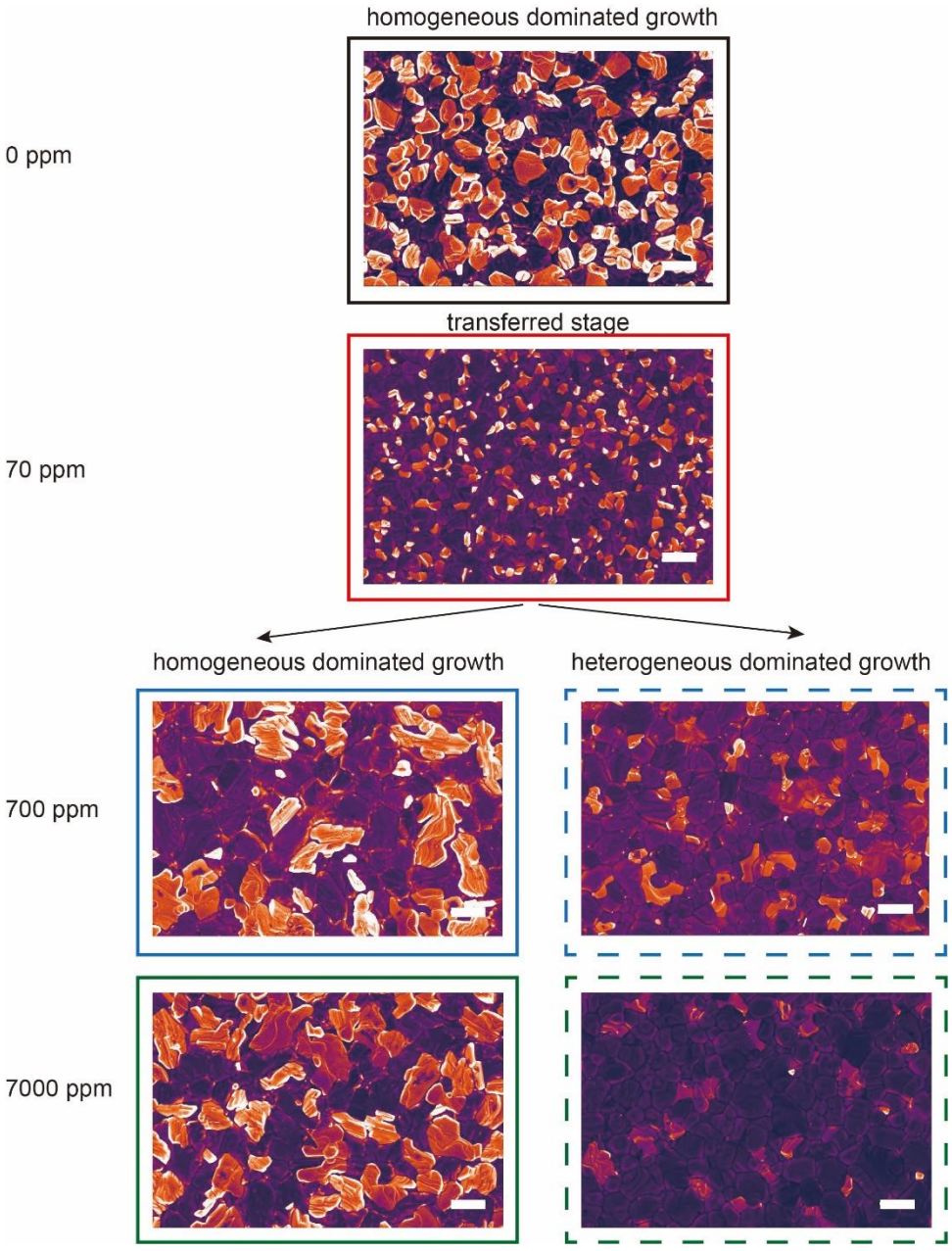

Figure S7. SEM images of annealed perovskite films.

False-colored SEM images of annealed perovskite films with 0 (black frame), 70 (red frame), 700 (blue frame), and 7000 (green frame) ppm water. A higher amount of water (> 700 ppm) in the perovskite films results in the appearance of a homogenous nucleation area (more lead PbI_2 at the surface, frames with dash lines) and a heterogeneous nucleation area (less PbI_2 at the surface, frames with solid lines). The bright areas indicate the formation of PbI_2, according to previous reports.[12] The scale bar is one μm.

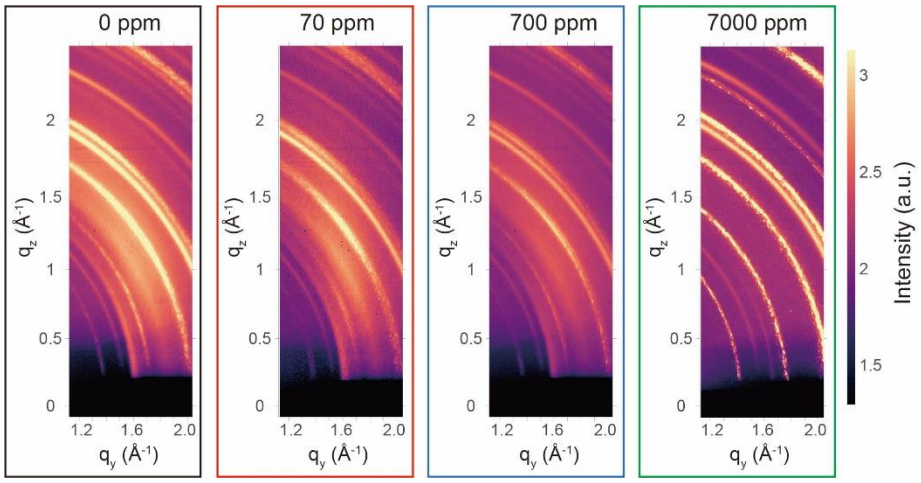

Figure S8.

2D GIWAXS data of perovskite films with 0 ppm (black), 70 ppm (red), 700 ppm (blue), and 7000 ppm (green) water. The grey frame indicates the integration area of 2D GIWAXS images.

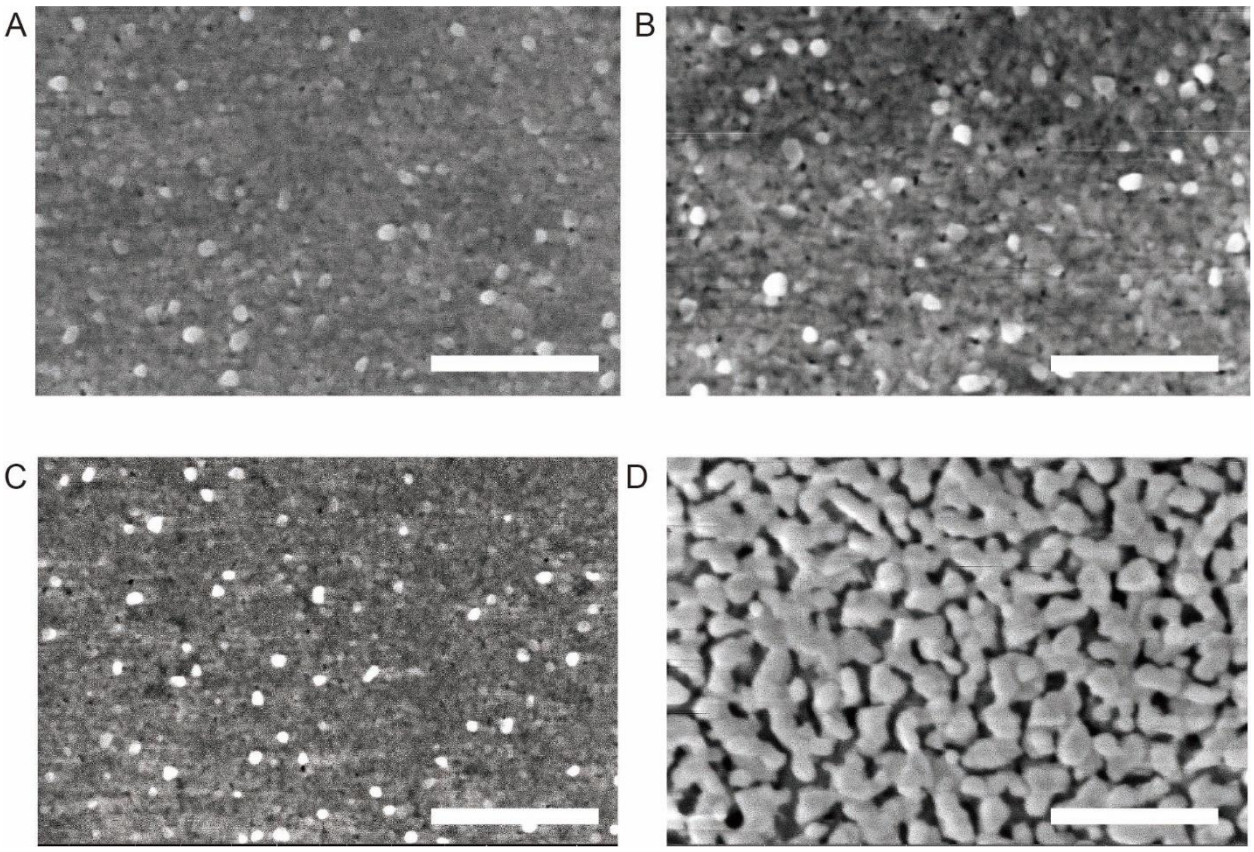

Figure S9.

SEM images of PbI_2 films with 0 (A), 70 (B), 700 (C), and 7000 (D) ppm water. The scale bar is 1 μm.

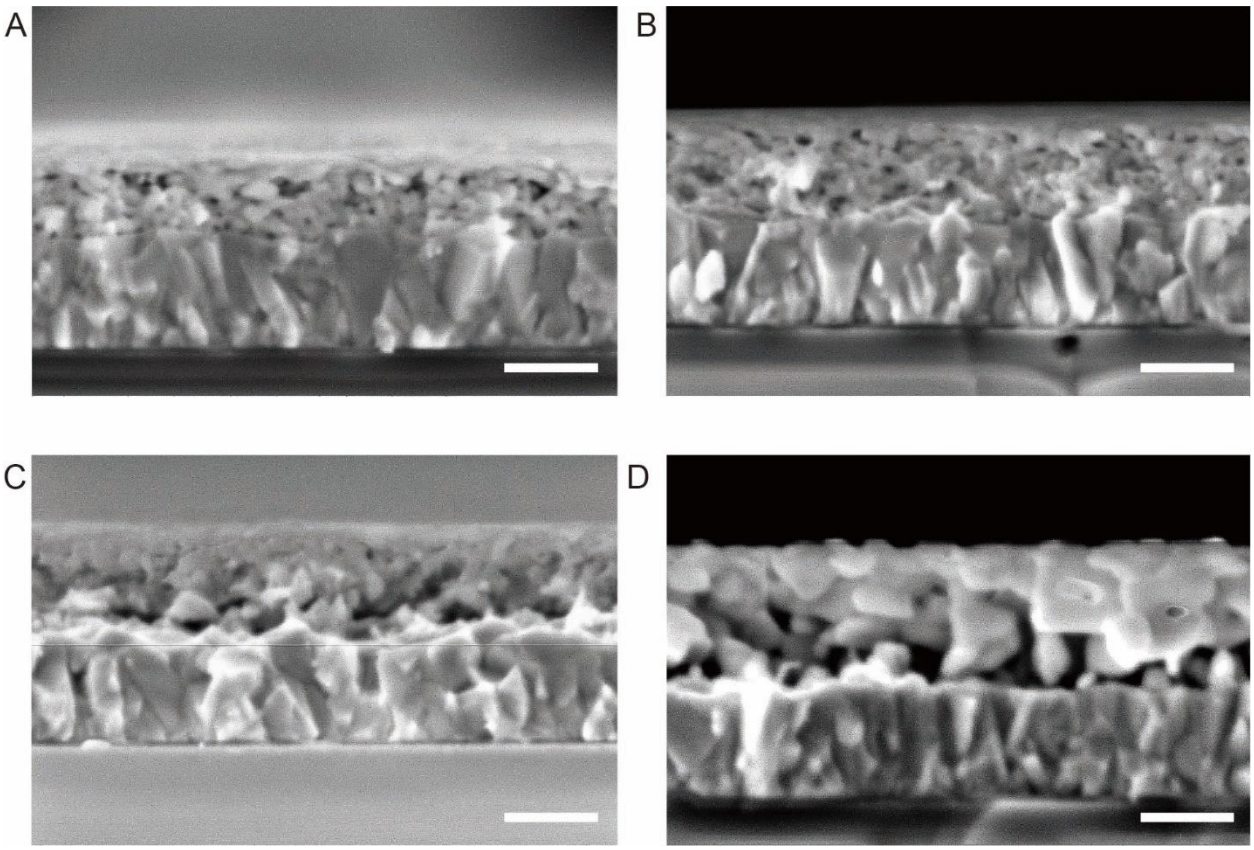

Figure S10.

Cross-section SEM images of PbI_2 films with 0 (A), 70 (B), 700 (C), and 7000 (D) ppm water. The scale bar is 500 nm.

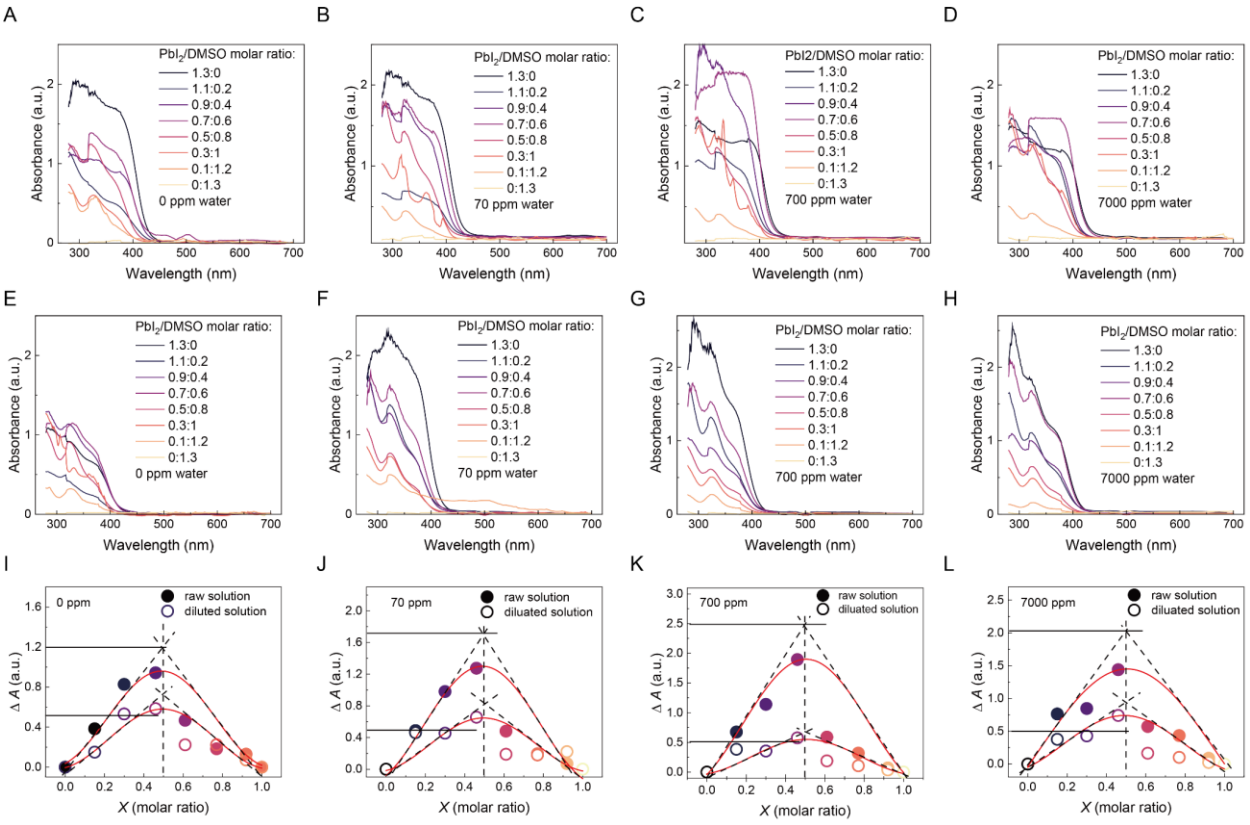

Figure S11. Light absorption spectra and continuous variation plots of PbI_2 and DMSO complex with different water content.

(A)Light absorption of 1.3 M PbI_2/DMSO in DMF solution with 0 ppm water; (B) light absorption of 1.3 M PbI_2/DMSO in DMF solution with 70 ppm water; (C) light absorption of 1.3 M PbI_2/DMSO in DMF solution with 700 ppm water; (D) light absorption of 1.3 M PbI_2/DMSO in DMF solution with 7000 ppm water; (E) light absorption of 0.65 M PbI_2/DMSO in DMF solution with 0 ppm water; (F) light absorption of 0.65 M PbI_2/DMSO in DMF solution with 70 ppm water; (G) light absorption of 0.65 M PbI_2/DMSO in DMF solution with light absorption of 0.65 M PbI_2/DMSO in DMF solution with diluted 700 ppm water; (H) light absorption of 0.65 M PbI_2/DMSO in DMF solution with 700 ppm water; (I) continuous variation curve for PbI_2/DMSO in DMF solution with 0 ppm water; (J) continuous variation curve for PbI_2/DMSO in DMF solution with 70 ppm water; (K) continuous variation curve for PbI_2/DMSO in DMF solution with 700 ppm water; (L) continuous variation curve for PbI_2/DMSO in DMF solution with 7000 ppm water.

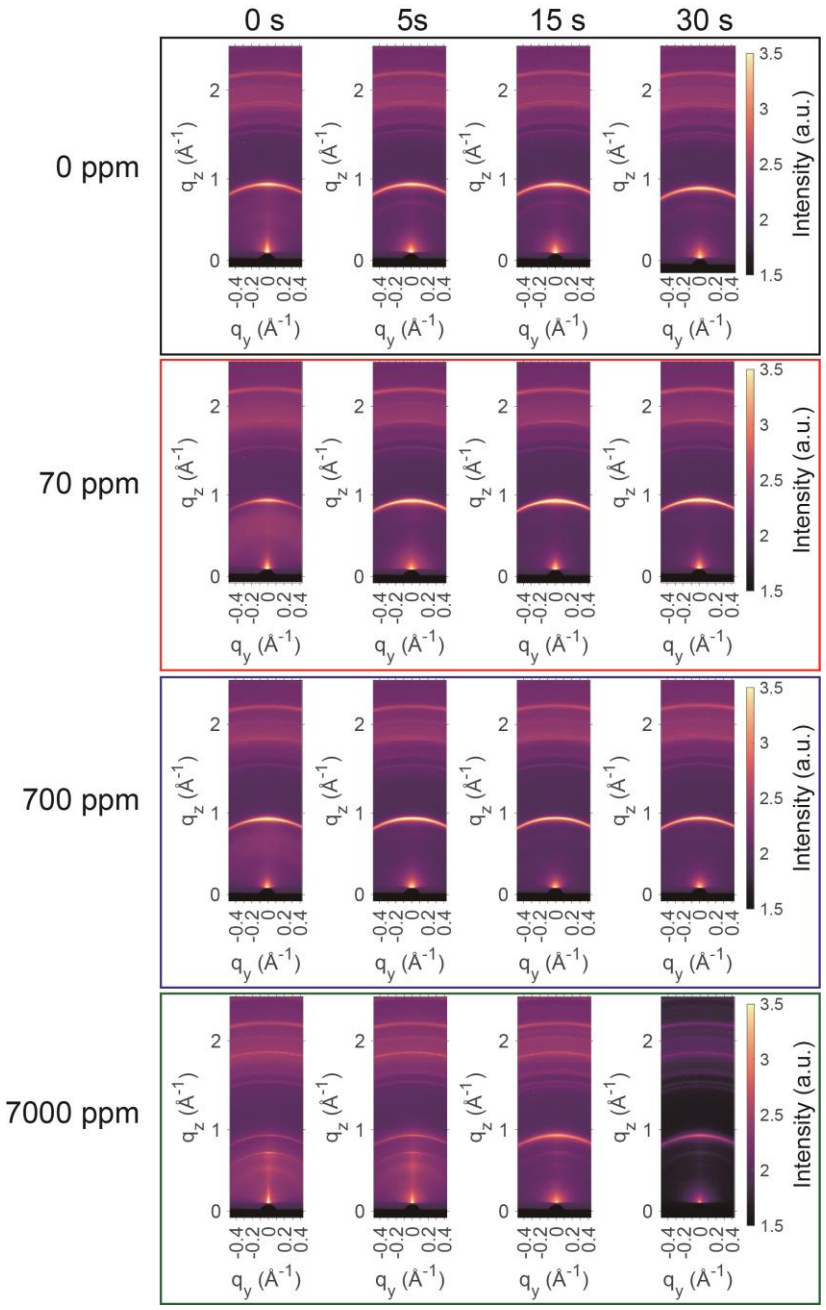

Figure S12.

Temporal evolution of 2D GIWAXS data for lead iodide films with 0, 70, 700, 7000 ppm water in situ annealed at 70 °C. (A) 0 ppm; (B) 70 ppm; (C) 700 ppm; (D) 7000 ppm.

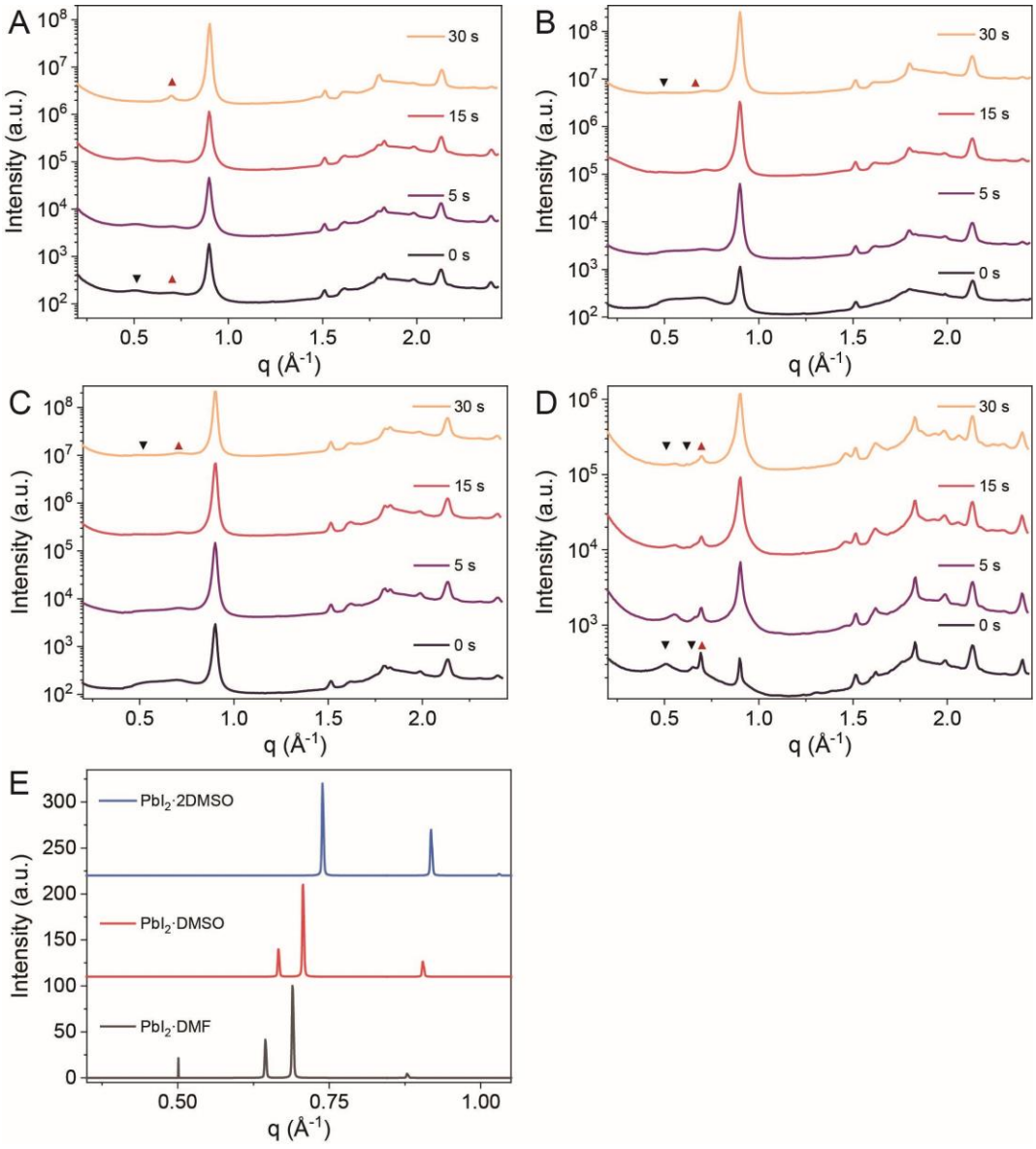

Figure S13. Temporal evolution of pseudo-X-ray diffraction patterns extracted from 2D GIWAXS data for lead iodide films with 0, 70, 700, 7000 ppm water in situ annealed at 70 °C.

(A) 0 ppm; (B) 70 ppm; (C) 700 ppm; (D) 7000 ppm; (E) X-ray diffraction patterns calculated from the standard structures of different lead iodide complexes and related structure cif-files are offered in supplementary files and subtracted from literature.[13-16] The black inverted triangle symbol indicates PbI_2·DMF phase, and the red triangle symbol indicates PbI_2·DMSO phase.

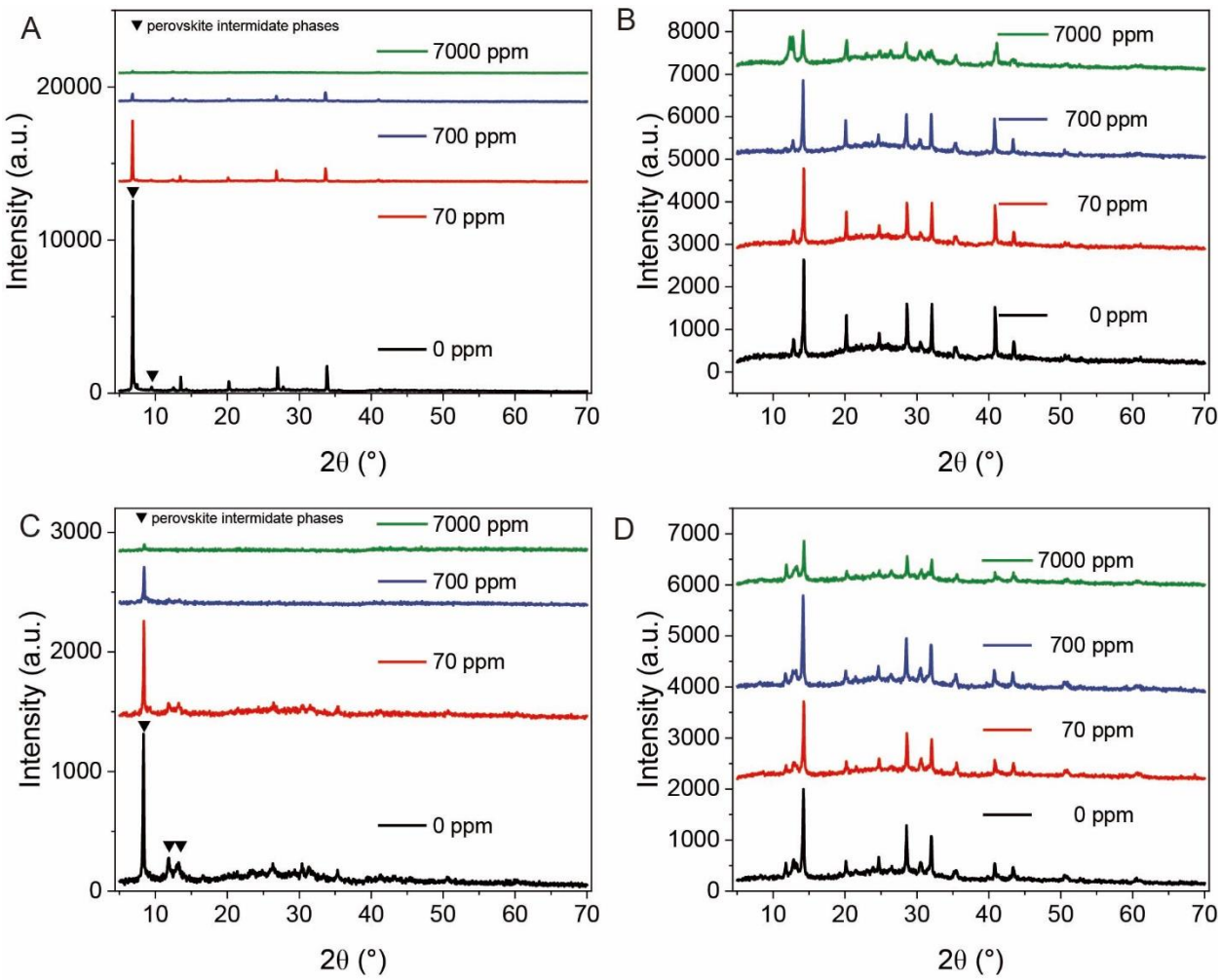

Figure S14.

XRD patterns of perovskite precursor inks (1.2 M) with different additives for wet and dry films on the ITO /glass substrates: (A) wet film of $(MAPbBr_3)_{0.17}(FAPbI_3)_{0.83}$-DMF/DMSO; (B) dry film of $(MAPbBr_3)_{0.17}(FAPbI_3)_{0.83}$-DMF/DMSO; (C) wet film of $(MAPbBr_3)_{0.17}(FAPbI_3)_{0.83}$-DMF/NMP; (D) dry film of $(MAPbBr_3)_{0.17}(FAPbI_3)_{0.83}$-DMF/NMP.

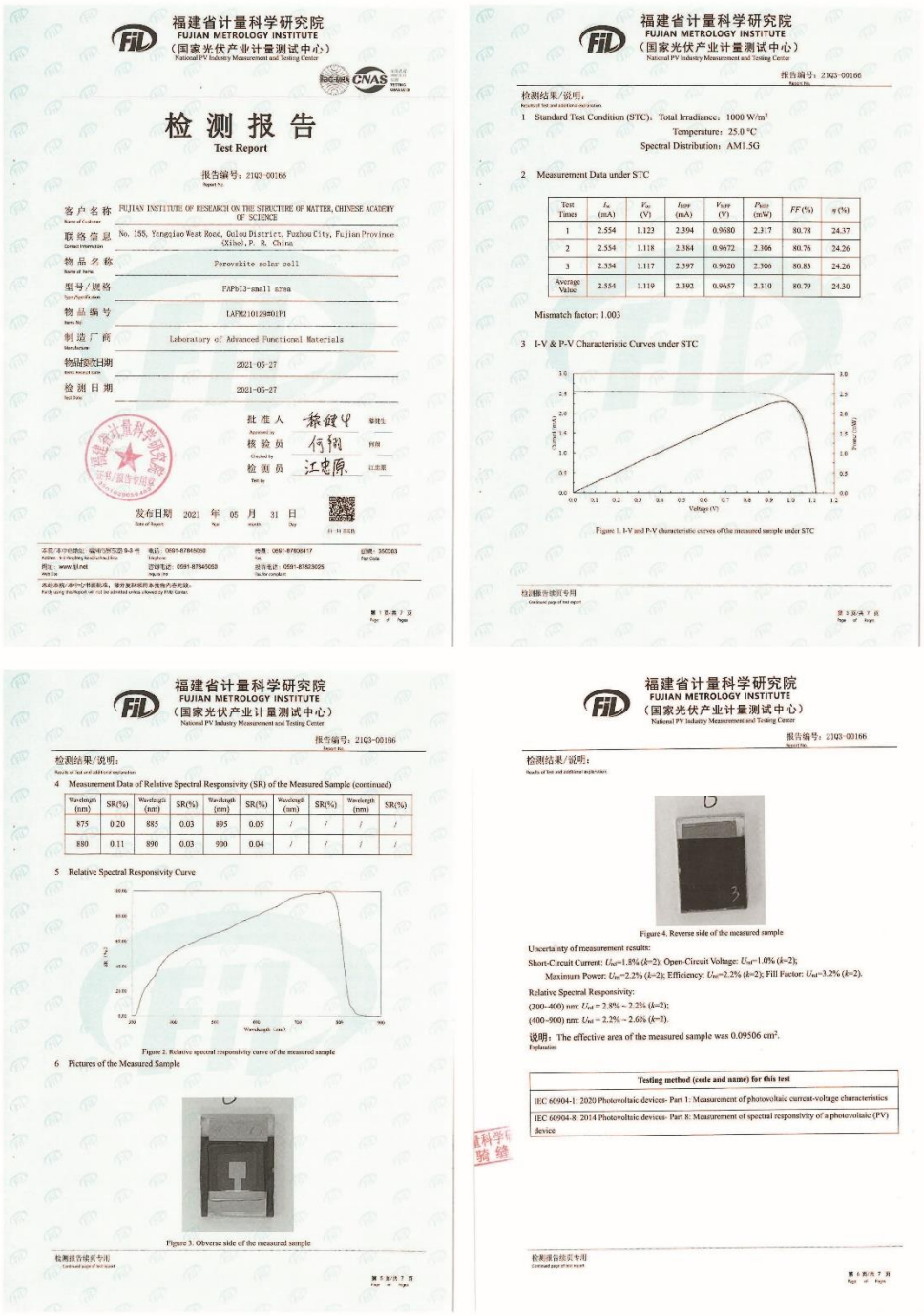

福建省计量科学研究院
FUJIAN METROLOGY INSTITUTE
（国家光伏产业计量测试中心）
National PV Industry Measurement and Testing Center

检 测 报 告
Test Report

报告编号：21Q3-00166

客户名称	FUJIAN INSTITUTE OF RESEARCH ON THE STRUCTURE OF MATTER, CHINESE ACADEMY OF SCIENCE
联络信息	No. 155, Yangqiao West Road, Gulou District, Fuzhou City, Fujian Province (Xibei), P. R. China
物品名称	Perovskite soler cell
型号/规格	FAPbI3-small area
物品编号	LAFM210129B01P1
制造厂商	Laboratory of Advanced Functional Materials
物品收样日期	2021-05-27
检测日期	2021-05-27

批准人 核验员 检测员

发布日期 2021 年 05 月 31 日

检测结果/说明：

1 Standard Test Condition (STC): Total Irradiance: 1000 W/m²
Temperature: 25.0 °C
Spectral Distribution: AM1.5G

2 Measurement Data under STC

Test Times	I_{sc} (mA)	V_{oc} (V)	I_{MPP} (mA)	V_{MPP} (V)	P_{MPP} (mW)	FF (%)	η (%)
1	2.554	1.123	2.394	0.9680	2.317	80.78	24.37
2	2.554	1.118	2.384	0.9672	2.306	80.76	24.26
3	2.554	1.117	2.397	0.9620	2.306	80.83	24.26
Average Value	2.554	1.119	2.392	0.9657	2.310	80.79	24.30

Mismatch factor: 1.003

3 I-V & P-V Characteristic Curves under STC

Figure 1. I-V and P-V characteristic curves of the measured sample under STC

4 Measurement Data of Relative Spectral Responsivity (SR) of the Measured Sample (continued)

Wavelength (nm)	SR(%)	Wavelength (nm)	SR(%)	Wavelength (nm)	SR(%)	Wavelength (nm)	SR(%)	Wavelength (nm)	SR(%)
875	0.20	885	0.03	895	0.05	/	/	/	/
880	0.11	890	0.03	900	0.04	/	/	/	/

5 Relative Spectral Responsivity Curve

Figure 2. Relative spectral responsivity curve of the measured sample

6 Pictures of the Measured Sample

Figure 3. Obverse side of the measured sample

Figure 4. Reverse side of the measured sample

Uncertainty of measurement results:
Short-Circuit Current: U_{rel}=1.8% (k=2); Open-Circuit Voltage: U_{rel}=1.0% (k=2);
Maximum Power: U_{rel}=2.2% (k=2); Efficiency: U_{rel}=2.2% (k=2); Fill Factor: U_{rel}=3.2% (k=2).

Relative Spectral Responsivity:
(300–400) nm: U_{rel} = 2.8% ~ 2.2% (k=2);
(400–900) nm: U_{rel} = 2.2% ~ 2.6% (k=2).

说明：The effective area of the measured sample was 0.09506 cm².

Testing method (code and name) for this test
IEC 60904-1: 2020 Photovoltaic devices- Part 1: Measurement of photovoltaic current-voltage characteristics
IEC 60904-8: 2014 Photovoltaic devices- Part 8: Measurement of spectral responsivity of a photovoltaic (PV) device

Figure S15.

Certification by the National Photovoltaic Industry Metrology and Testing Center (NPVM, China), one of the designated test centers for *solar cell efficiency tables*. The PSC has a PCE of 24.30 % with an aperture area of 0.09506 cm^2. A PDF version is attached in Supporting Document 1.

Figure S16.

Certification by the National Photovoltaic Industry Metrology and Testing Center (NPVM, China), one of the designated test centers for *solar cell efficiency tables*. The PSC has a PCE of 22.71 % with an aperture area of 1.0036 cm^2. A PDF version is attached in Supporting Document 2.

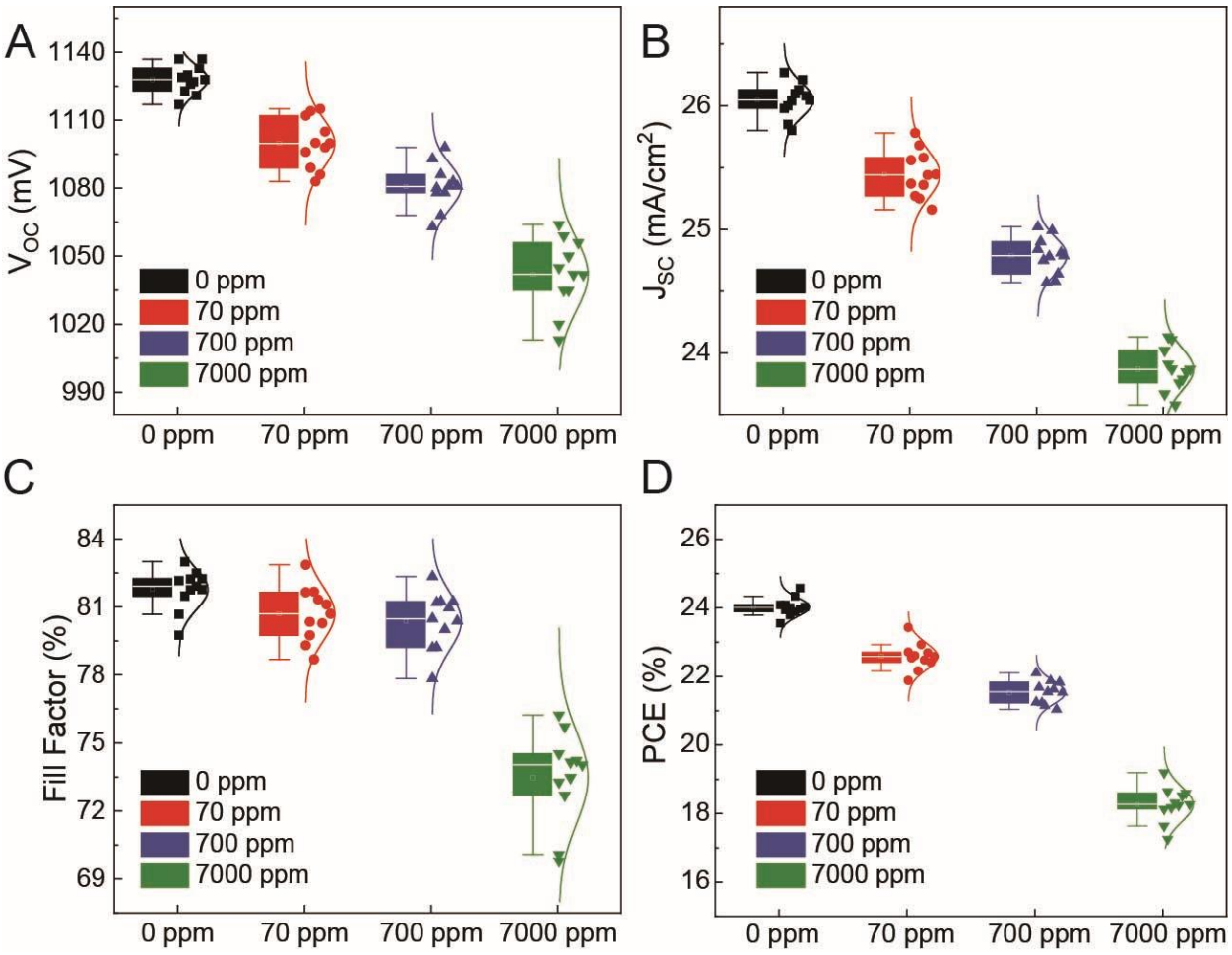

Figure S17.

Device statistics are shown in box plots (center line: average; box limit: standard deviation; whiskers: outliers) for (A) open-circuit voltage, (B) short-circuit current, (C) fill factor, (D) power conversion efficiency for solar cells with water contents of 0 ppm (black), 70 ppm (red), 700 ppm (blue), and 7000 ppm (green).

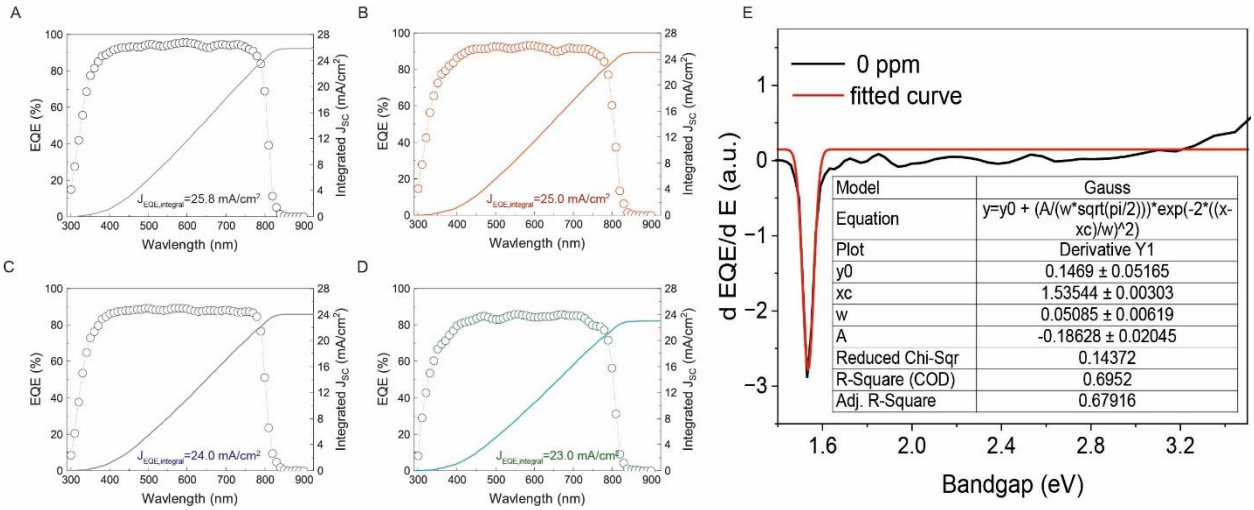

Figure S18.

External quantum efficiency (EQE) and integrated short-circuit current J_{SC} for perovskite solar cells with 0 ppm (black), 70 ppm (red), 700 ppm (blue), and 7000 ppm (green) water contents. (E)The first derivative of EQE spectra of perovskite solar cells fabricated by 0 ppm water content PbI_2. The J_{SC} mismatch between our EQE and *J-V* characterization is 3.7 %.[17]

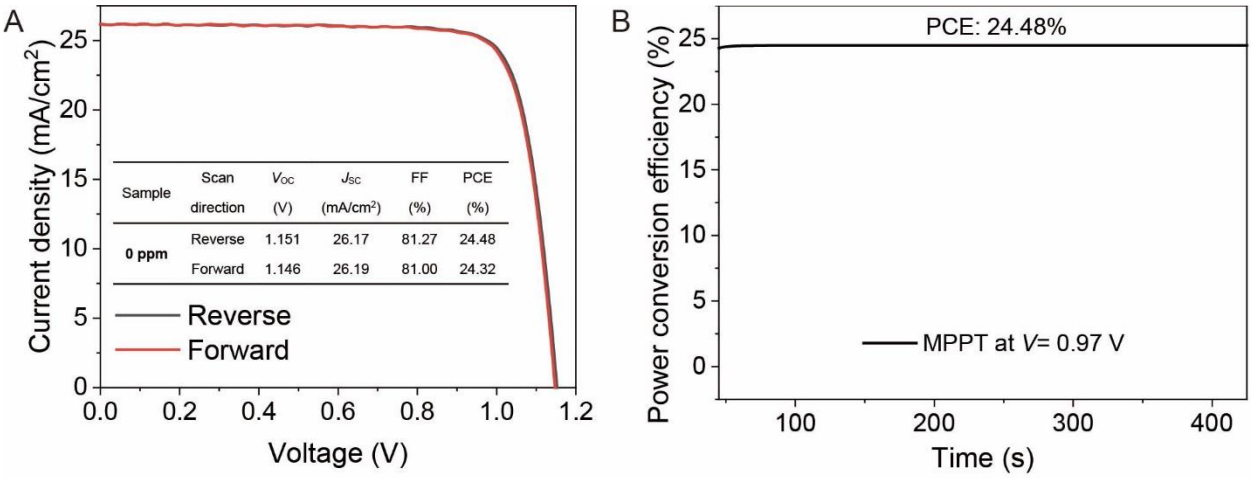

Sample	Scan direction	V_{OC} (V)	J_{SC} (mA/cm^2)	FF (%)	PCE (%)
0 ppm	Reverse	1.151	26.17	81.27	24.48
	Forward	1.146	26.19	81.00	24.32

Figure S19.

(A) J-V scan of perovskite solar cells fabricated by 0 ppm; (B)400-s MPPT tracking data of perovskite solar cells fabricated by 0 ppm.

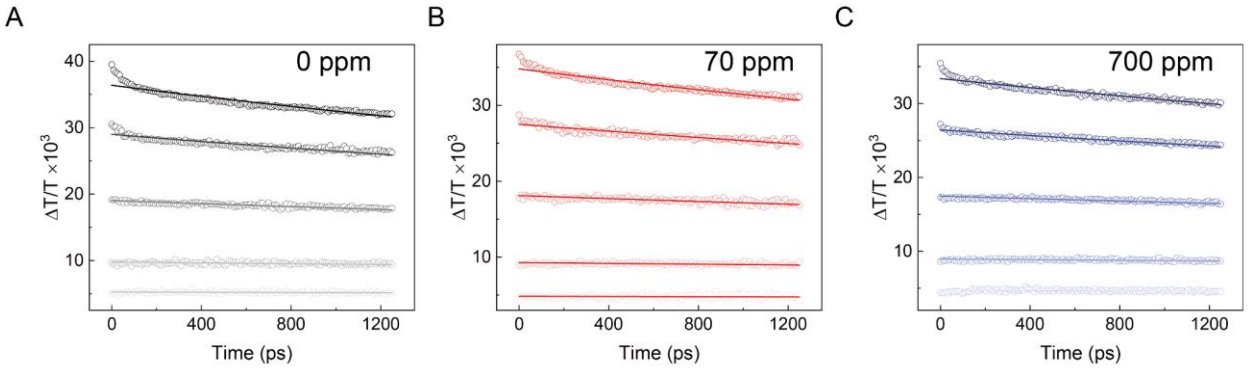

Figure S20. Photo-induced terahertz conductivity transient spectra.

Photo-induced terahertz conductivity transients were monitored over a 1 ns window following pulsed (15 fs) excitation at 400 nm with a range of pulse fluences for different perovskite films. (A) 0 ppm water; (B) 70 ppm water; (C) 700 ppm water.

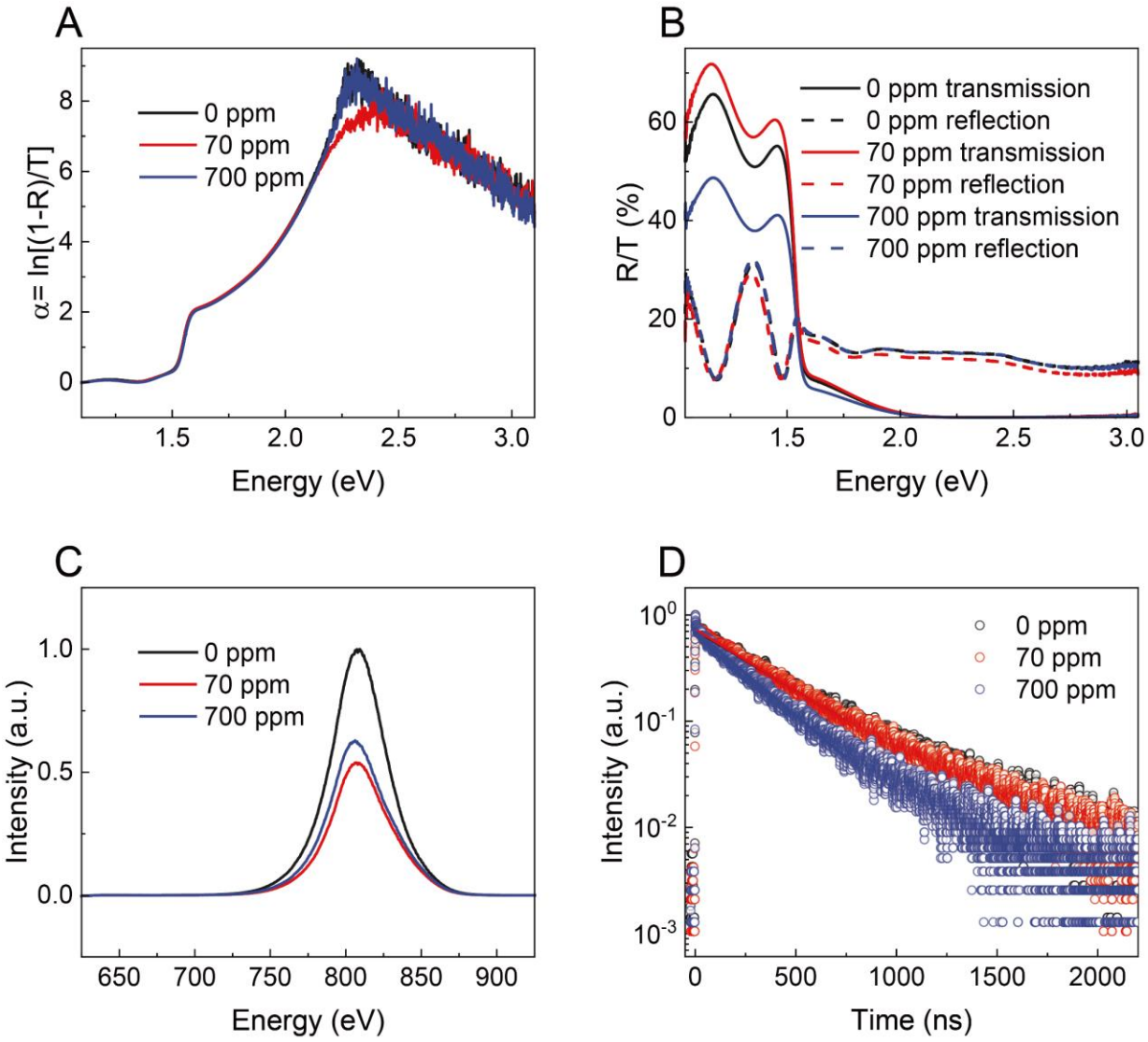

Figure S21. Photo-induced terahertz conductivity transient spectra.

(A) Absorption spectra of different perovskite films obtained from FTIR spectrometry; (B) fractions of the reflected and transmitted light through different perovskite films; (C) steady-state photoluminescence spectra of different perovskite films; (D) time-resolved photoluminescence spectra measured with the time-correlated single-photon counting technique for perovskite films with different amounts of water.

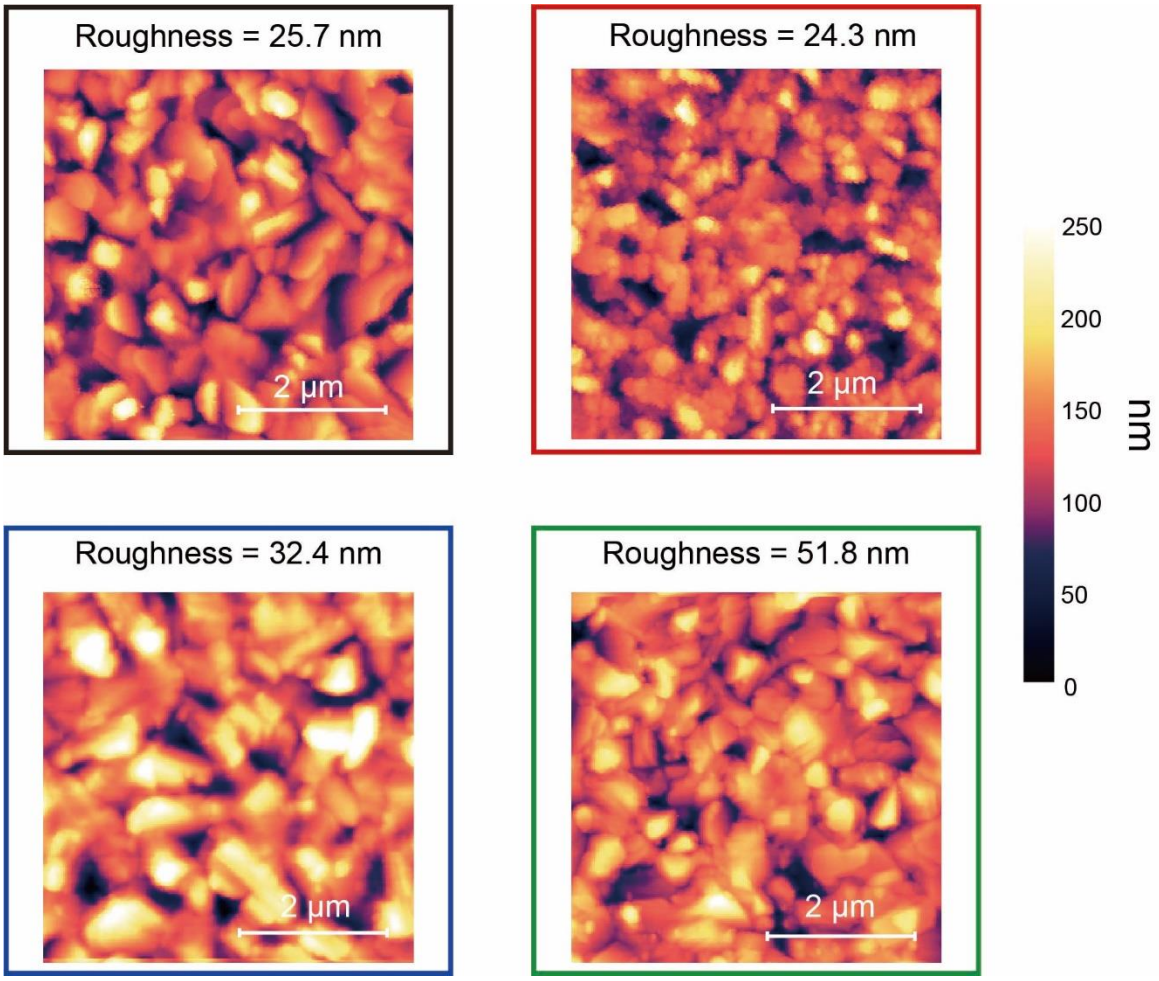

Figure S22. AFM data from perovskite thin film samples.

AFM images were obtained from the perovskite films with 0 ppm (black), 70 ppm (red), 700 ppm (blue), and 7000 ppm (green) water. The scale bar is 2 µm.

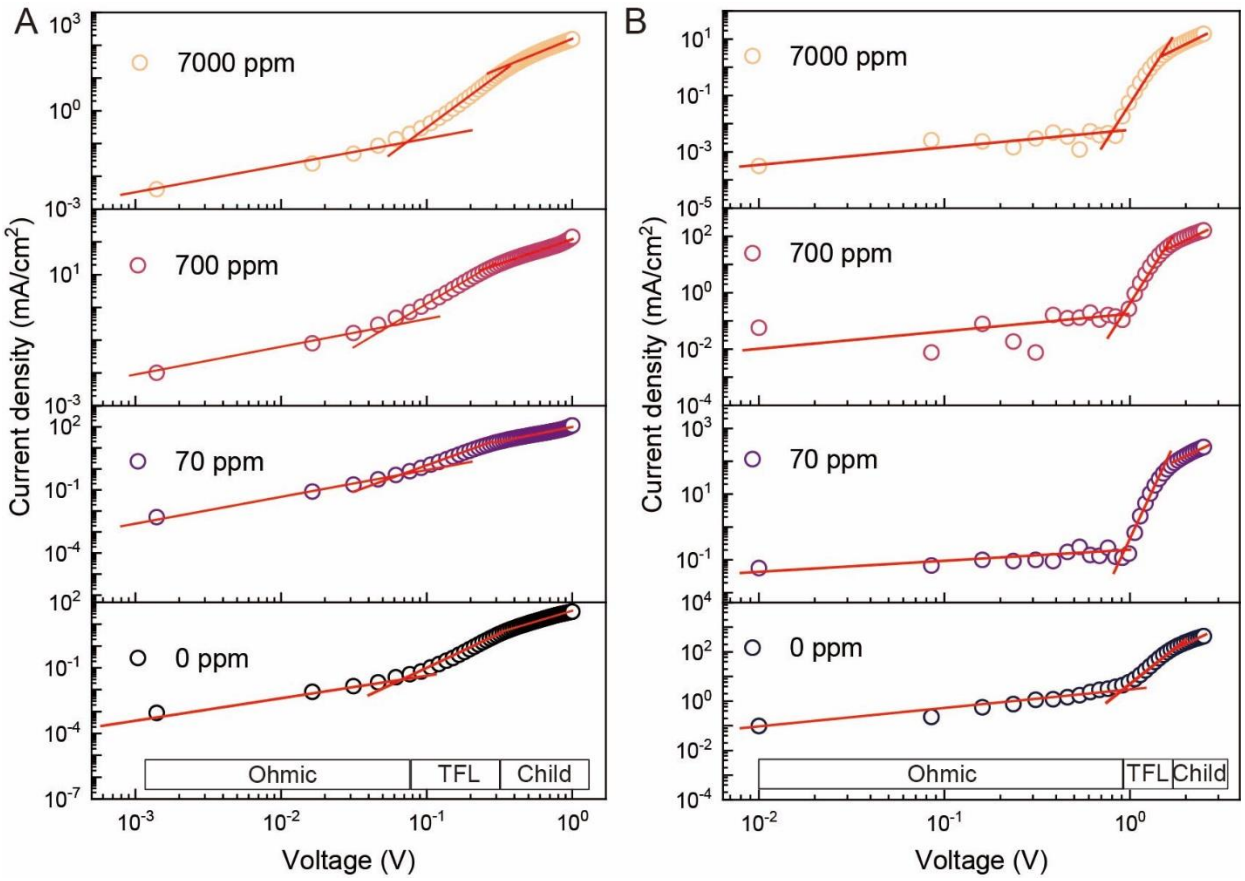

Figure S23. Evolution of *J-V* (log scale) curves from measuring SCLC with different water contents perovskite films.

(A) electron-only devices; (B) hole-only devices.

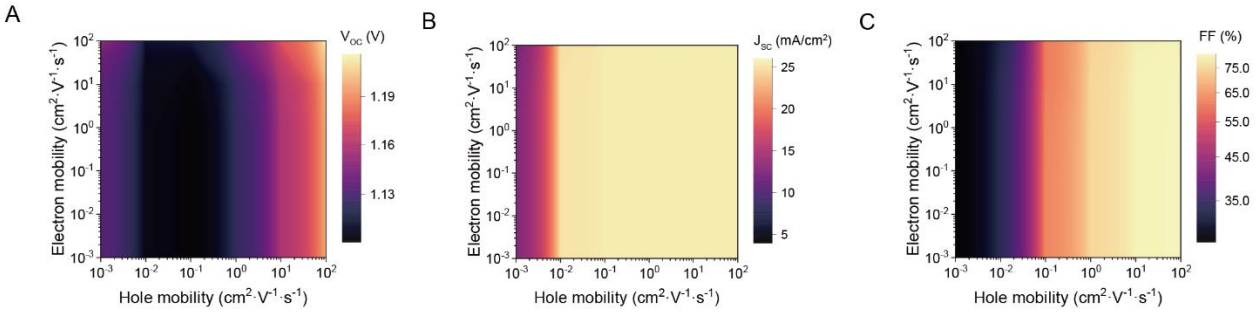

Figure S24. Extended Data Fig. 10. Dependence of device performance simulation through the "drift-diffusion" model with different electron and hole mobilities.

Dependence of device performance simulation through the "drift-diffusion" model with different electron and hole mobilities. (A) Dependence of open-circuit voltage with different electron and hole mobilities; (B) dependence of short-circuit current with different electron and hole mobilities; (C) dependence of fill factor on different electron and hole mobilities.

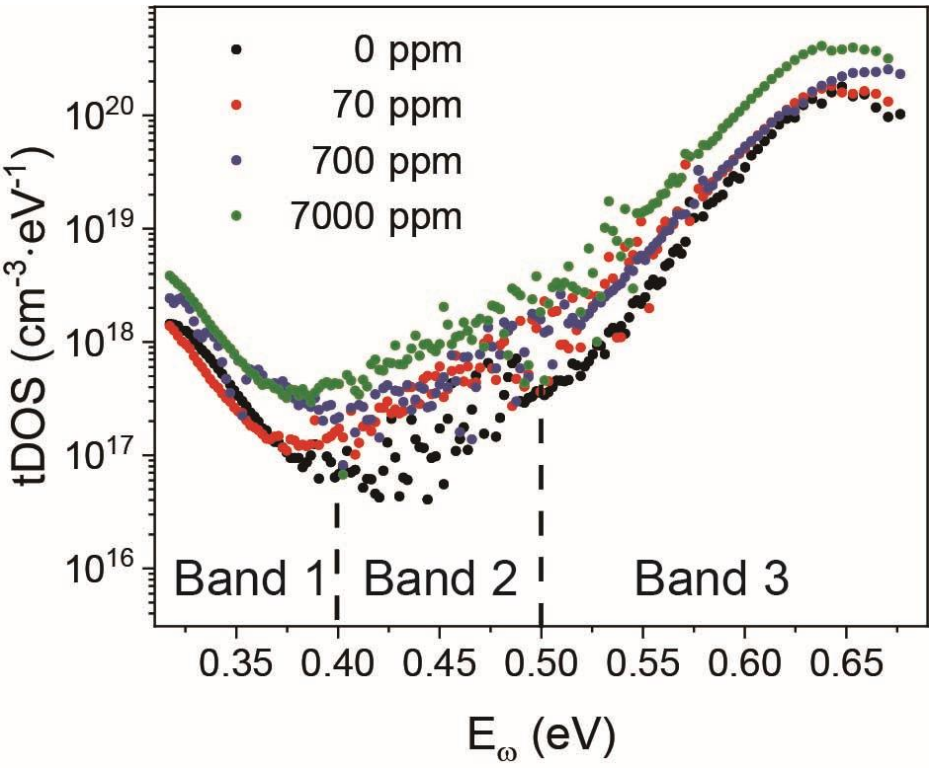

Figure S25.

Trap density of states (tDOS) obtained by thermal admittance spectroscopy for perovskite with 0 ppm (black), 70 ppm (red), 700 ppm (blue), and 7000 ppm (green) water contents.

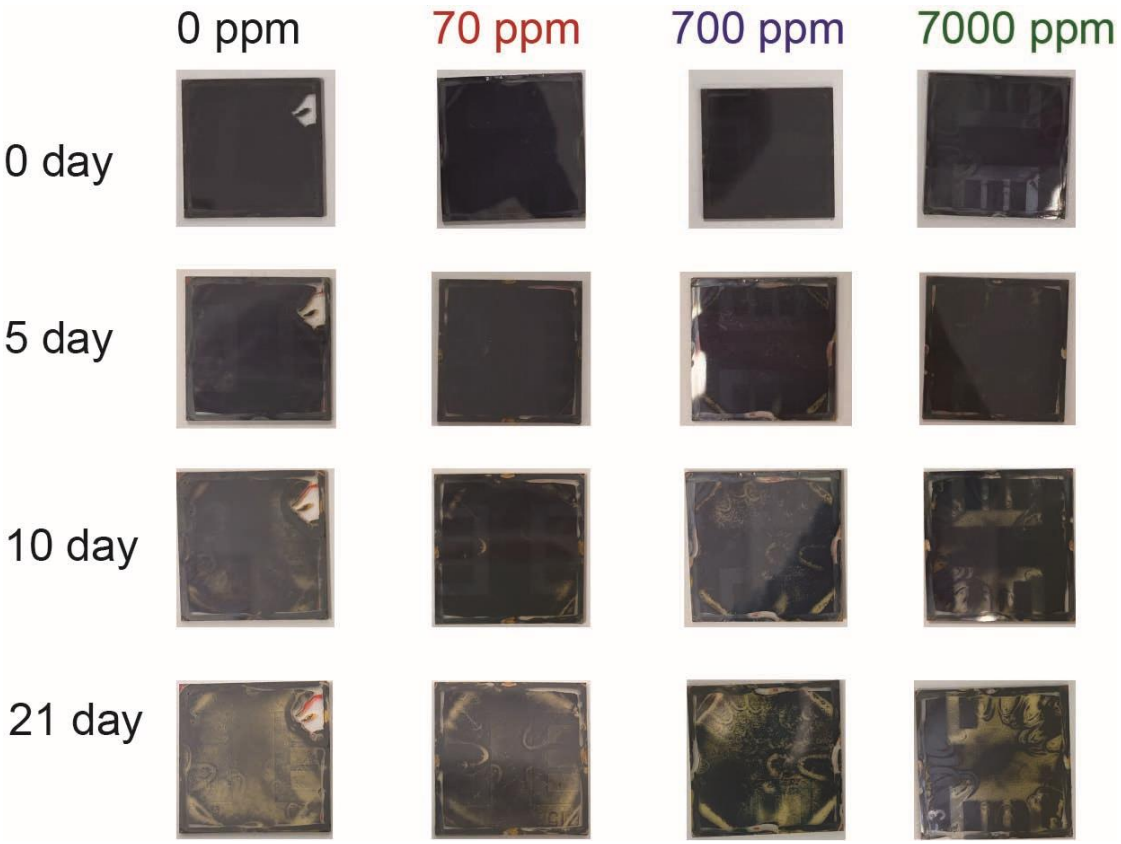

Figure S26.

Degradation photographs of the perovskite films with 0 ppm (black), 70 ppm (red), 700 ppm (blue), and 7000 ppm (green) water under RH 40 % condition.

Table S1. Detailed comparison of different PbI_2 synthesized by solution method (type I) and thermal annealing method (type II)

Brand	Purity (%)	Water content (ppm)*	Storage	Price (g/$)
I	99.999	<50	brown glass bottle	2.76
II	99.999	AnhydroBeads	ampule	16.88

* The information is subtracted from their product specifications.

Table S2. 1.3 M PbI_2 solution with different DMF/DMSO ratios.

Sample	1	2	3	4	5	6	7	8
PbI_2	1.3	1.1	0.9	0.7	0.5	0.3	0.1	0
DMSO	0	0.2	0.4	0.6	0.8	1	1.2	1.3
DMF	3	3	3	3	3	3	3	3

Table S3. 0.65 M PbI_2 solution with different DMF/DMSO ratios.

Sample	1	2	3	4	5	6	7	8
PbI_2	1.3	1.1	0.9	0.7	0.5	0.3	0.1	0
DMSO	0	0.2	0.4	0.6	0.8	1	1.2	1.3
DMF	6	6	6	6	6	6	6	6

Table S4. Non-isothermal crystallization kinetic parameters of perovskite-related intermediate phases by using the Jeziorny equation.

	Heating rate (℃/s)	0 ppm	70 ppm	700 ppm	7000 ppm
n	0.8	1.11	0.98	0.82	0.77
	0.5	0.68	0.81	0.72	0.07
***n* (avg)**	0.4	0.90	0.985	0.77	0.42
Z_c	0.8	3.75×10^{-3}	1.25×10^{-2}	4.30×10^{-2}	2×10^{-1}
	0.5	5.32×10^{-2}	6.22×10^{-2}	7.94×10^{-2}	3.24×10^{-1}
R^2	0.8	0.99	0.99	0.99	0.99
	0.5	0.99	0.99	1.00	0.99

Table S5. Perovskite parameters

Description	Parameters
Thickness (nm)	600
Bandgap (eV)	1.6
Electron affinity (eV)	3.9
Dielectric permittivity (relative)	23
CB effective density of state ($1 \cdot cm^{-3}$)	7.79×10^{18}
VB effective density of state ($1 \cdot cm^{-3}$)	2.37×10^{20}
Electron thermal velocity ($cm \cdot s^{-1}$)	10^{7}
Hole thermal velocity ($cm \cdot s^{-1}$)	10^{7}
Electron mobility ($cm^{2} \cdot V^{-1} \cdot s^{-1}$)	22
Hole mobility ($cm^{2} \cdot V^{-1} \cdot s^{-1}$)	22
The effective mass of electrons	0.1
The effective mass of holes	0.21
Radiative recombination coefficient ($cm^{3} \cdot s^{-1}$)	3.16×10^{-12}

Table. S6 Spiro-OMeTAD parameters

Description	Parameters
Thickness (nm)	200
Bandgap (eV)	3.1
Electron affinity (eV)	2.1
Dielectric permittivity (relative)	4
CB effective density of state ($1 \cdot cm^{-3}$)	2.5×10^{18}
VB effective density of state ($1 \cdot cm^{-3}$)	1.8×10^{19}
Electron thermal velocity ($cm \cdot s^{-1}$)	10^{7}
Hole thermal velocity ($cm \cdot s^{-1}$)	10^{7}
Electron mobility ($cm^{2} \cdot V^{-10} \cdot s^{-1}$)	0.02
Hole mobility ($cm^{2} \cdot V^{-1} \cdot s^{-1}$	0.02

Table S7. SCLC parameters

Description	Parameters
Thickness (nm)	800
Dielectric permittivity (relative)	23
Vacuum permittivity ($F \cdot m^{-1}$)	8.85×10^{-12}
Area of electrode (cm^2)	0.03

Table S8. Extracted perovskite electron and hole mobility from SCLC measurements

Perovskite devices with different water contents in PbI_2 precursor	Electron mobility ($cm^2 \cdot V^{-1} \cdot s^{-1}$)	Hole mobility ($cm^2 \cdot V^{-1} \cdot s^{-1}$)
0 ppm	17.95	22.64
70 ppm	16.53	21.56
700 ppm	13.69	4.99
7000 ppm	12.59	0.23

References

[1] Y. Wu, A. Islam, X. Yang, C. Qin, J. Liu, K. Zhang, W. Peng, L. Han, *Energy & Environmental Science* **2014**, 7, 2934.

[2] M. Tinkham, *Physical Review* **1956**, 104, 845.

[3] J. Lloyd-Hughes, T.-I. Jeon, *Journal of Infrared, Millimeter, and Terahertz Waves* **2012**, 33, 871.

[4] A. M. Ulatowski, L. M. Herz, M. B. Johnston, *Journal of Infrared, Millimeter, and Terahertz Waves* **2020**, 41, 1431.

[5] C. L. Davies, J. B. Patel, C. Q. Xia, L. M. Herz, M. B. Johnston, *Journal of Infrared, Millimeter, and Terahertz Waves* **2018**, 39, 1236.

[6] V. D'Innocenzo, G. Grancini, M. J. P. Alcocer, A. R. S. Kandada, S. D. Stranks, M. M. Lee, G. Lanzani, H. J. Snaith, A. Petrozza, *Nature Communications* **2014**, 5, 3586.

[7] L. M. Herz, *Annual review of physical chemistry* **2016**, 67, 65.

[8] T. W. Crothers, R. L. Milot, J. B. Patel, E. S. Parrott, J. Schlipf, P. Müller-Buschbaum, M. B. Johnston, L. M. Herz, *Nano Letters* **2017**, 17, 5782.

[9] J. A. Röhr, *Physical Review Applied* **2019**, 11, 054079.

[10] V. M. Le Corre, E. A. Duijnstee, O. El Tambouli, J. M. Ball, H. J. Snaith, J. Lim, L. J. A. Koster, *ACS energy letters* **2021**, 6, 1087.

[11] E. A. Duijnstee, J. M. Ball, V. M. Le Corre, L. J. A. Koster, H. J. Snaith, J. Lim, *ACS Energy Letters* **2020**, 5, 376.

[12] Q. Jiang, Z. Chu, P. Wang, X. Yang, H. Liu, Y. Wang, Z. Yin, J. Wu, X. Zhang, J. You, *Advanced materials* **2017**, 29, 1703852.

[13] D. Barrit, P. Cheng, M. C. Tang, K. Wang, H. Dang, D. M. Smilgies, S. Liu, T. D. Anthopoulos, K. Zhao, A. Amassian, *Advanced Functional Materials* **2019**, 29, 1807544.

[14] T. Bu, J. Li, H. Li, C. Tian, J. Su, G. Tong, L. K. Ono, C. Wang, Z. Lin, N. Chai, *Science* **2021**, 372, 1327.

[15] D. Barrit, A. D. Sheikh, R. Munir, J. M. Barbé, R. Li, D.-M. Smilgies, A. Amassian, *Journal of Materials Research* **2017**, 32, 1899.

[16] D. Barrit, M.-C. Tang, R. Munir, R. Li, K. Zhao, D.-M. Smilgies, *ACS Applied Materials & Interfaces* **2022**.

[17] M. Saliba, E. Unger, L. Etgar, J. Luo, T. J. Jacobsson, *Nature Communications* **2023**, 14, 5445.